Measurement of proton-carbon forward scattering in a proof-of-principle test of the EMPHATIC spectrometer

M. Pavin[9] L. Aliaga-Soplin,[2] M. Barbi,[8] L. Bellantoni,[2] S. Bhadra,[11] B. Ferrazzi,[8] L. Fields,[2,7] A. Fiorentini,[11,*]
T. Fukuda,[6] K. Gameil,[9,†] Y. Al Hakim,[9,‡] M. Hartz,[9,4] B. Jamieson,[10] M. Kiburg,[2] N. Kolev,[8] H. Kawai,[1]
A. Konaka,[9] P. Lebrun,[2] T. Lindner,[9] T. Mizuno,[1] N. Naganawa,[6] J. Paley,[2] R. Rivera,[2] G. Santucci,[11] O. Sato,[6]
T. Sekiguchi,[3] A. Sikora,[10,§] G. Slater,[9] A. Suzuki,[5] T. Sugimoto,[5] M. Tabata,[1] L. Uplegger,[2] and T. Vladisavljevic[4,‖]

(EMPHATIC Collaboration)

[1]*Department of Physics, Chiba University, Chiba, Chiba 263-8522, Japan*
[2]*Fermi National Accelerator Laboratory, Batavia, Illinois 60510, USA*
[3]*Institute of Particle and Nuclear Study (IPNS), High Energy Accelerator Research Organization (KEK), Tsukuba 305-0801, Japan*
[4]*Kavli Institute for the Physics and Mathematics of the Universe (WPI),*
The University of Tokyo Institutes for Advanced Study, University of Tokyo, Kashiwa, Chiba 277-8583, Japan
[5]*Kobe University, Kobe, Hyogo 657-8501, Japan*
[6]*Nagoya University, Nagoya, Aichi 464-8601, Japan*
[7]*Department of Physics, University of Notre Dame, Notre Dame, Indiana 46556, USA*
[8]*Department of Physics, University of Regina, Regina, Saskatchewan S4S 0A2, Canada*
[9]*TRIUMF, Vancouver, British Columbia V6T 2A3, Canada*
[10]*University of Winnipeg, Winnipeg, Manitoba R3B 2E9, Canada*
[11]*Department of Physics and Astronomy, York University, Toronto, Ontario M3J 1P3, Canada*

The next generation of long-baseline neutrino experiments will be capable of precise measurements of neutrino oscillation parameters, precise neutrino-nucleus scattering, and unprecedented sensitivity to physics beyond the Standard Model. Reduced uncertainties in neutrino fluxes are necessary to achieve high precision and sensitivity in these future neutrino measurements. New measurements of hadron-nucleus interaction cross sections are needed to reduce uncertainties of neutrino fluxes. We report measurements of the differential cross section as a function of scattering angle for proton-carbon interactions with a single charged particle in the final state at beam momenta of 20, 30, and 120 GeV/c. These measurements are the result of a beam test for EMPHATIC, a hadron-scattering and hadron-production experiment. The total, elastic and inelastic cross sections are also extracted from the data and compared to previous measurements. These results can be used in current and future long-baseline neutrino experiments and demonstrate the feasibility of future measurements by an upgraded EMPHATIC spectrometer.

I. INTRODUCTION

Measurements of hadron interactions spanning 2 orders of magnitude (1–100 GeV/c) of incident particle momenta are of crucial importance for reducing the neutrino production modeling uncertainty in accelerator-based and atmospheric

neutrino experiments. Neutrino flux uncertainty is the dominant uncertainty in many neutrino measurements, including neutrino-nucleus cross-section measurements, sterile neutrino searches, and *CP* violation measurements in atmospheric neutrinos. Long-baseline neutrino experiments are entering a new era of precision with the future Hyper-Kamiokande [1] and DUNE [2] projects. Uncertainties in the energy dependence of the neutrino flux and cross section are among the most challenging systematic uncertainties in these neutrino experiments.

Neutrinos are produced by the decay of hadrons created in proton interactions in nuclei. Since it is extremely difficult and time consuming to measure the neutrino beam flux as a function of energy, Monte Carlo simulations based on hadron interactions and decays are used to make *a priori* predictions of the neutrino flux.

---

*Also at South Dakota School of Mines and Technology, Rapid City, South Dakota 57701, USA.
†Also at Carleton University, Ottawa, Ontario K1S 5B6, Canada.
‡Also at Imperial College London, London SW7 2BX, United Kingdom.
§Also at McGill University, Montreal, Quebec H3A 0G4, Canada.
‖Also at STFC, Rutherford Appleton Laboratory, Harwell Campus, Didcot OX11 0QX, United Kingdom.

112008-1

This approach is limited by the sparse hadron interaction data, often with significant errors, and hadron interactions are the dominant systematic uncertainty in neutrino flux prediction. Interpolation and extrapolation of hadron interaction cross sections using phenomenological models introduce additional uncertainties. Measurements of hadron interactions are used to constrain or scale the models to provide a more precise prediction of the neutrino flux. A good example of how data are used in neutrino flux simulations can be found in [3].

Many of the hadron interaction data relevant to GeV-energy neutrino flux predictions were taken in the second half of the twentieth century. Although these data are valuable, they are insufficient for precise neutrino flux predictions due to low phase space coverage, vague definitions of measured quantities (inelastic or production cross section), and lack of error covariances. In more recent years, experiments like NA61/SHINE [4–7], HARP [8,9], and MIPP [10–12] collected valuable data based on direct requests and input from the neutrino experiments. These data include cross-section and hadron production measurements for various targets and beam momenta. Even with these data, the typical neutrino flux uncertainty in the current generation of the accelerator-based neutrino experiments is between 5% and 15% due to limited phase space coverage and other sources of systematic uncertainty.

Neutrino flux uncertainty directly affects all measurements performed in a single (near) detector where far-to-near detector cancellation is not possible. In addition, reduction of the neutrino flux uncertainty is also important for neutrino oscillation measurements, particularly measurements of CP violation in the lepton sector. Constraining the ν_e/ν_μ ratio and measuring the ν_e cross section is of utmost importance for reducing systematic uncertainty in CP violation measurements in the Hyper-Kamiokande and DUNE experiments [1,13]. These cross sections will be measured in the intermediate water Cherenkov detector in Hyper-Kamiokande and the DUNE near detector. However, these measurements are limited by the neutrino flux uncertainty, and a reduction of this uncertainty to levels of 3% is necessary. Another example is CP violation measurement in atmospheric neutrinos, which is limited by neutrino flux uncertainty from sub-20 GeV/c cosmic ray (re)interactions with the atmosphere. The uncertainty of ν_μ and ν_e atmospheric neutrino fluxes is around 10%. Additionally, uncertainties for $\nu_\mu/\bar{\nu}_\mu$ and $\nu_e/\bar{\nu}_e$ flux ratios are 1–10% and about 8%, respectively [14]. These uncertainties are dominated by sub-20 GeV/c pion and kaon interactions in the atmosphere [14].

Several missing pieces of data are necessary to reduce the neutrino flux uncertainty in current and future accelerator-based and atmospheric neutrino experiments:

(1) Hadron production in sub-10 GeV pion and kaon interactions on carbon, aluminium, titanium, and iron,

(2) Hadron production in sub-20 GeV proton-air interactions (or equivalent targets),

(3) Measurements of coherent elastic and quasielastic interactions of hadrons for carbon, aluminum, titanium, and iron targets between 1 and 120 GeV/c,

(4) Measurements of strange hadron production in proton-carbon interactions to validate older measurements.

A detailed explanation of each point is out of the scope of this paper and can be found in [15]. This paper describes a measurement of coherent elastic proton-carbon scattering made possible using data from an early beam test of the experiment to measure the production of hadrons at a testbeam in Chicagoland (EMPHATIC). Future EMPHATIC measurements will address the remaining items on the list.

II. EMPHATIC EXPERIMENT

EMPHATIC is designed to study hadron interactions in the 2–120 GeV/c range at the Fermilab Test Beam Facility (FTBF). The physics program of EMPHATIC covers previously listed requirements for improvement of neutrino flux in upcoming long-baseline neutrino oscillation experiments [15].

The EMPHATIC design exploits ~10 μm spatial resolution of silicon strip detectors resulting in a compact hadron spectrometer. The experiment's dipole magnet is a custom-built Halbach array of NdFeB magnets with bending power of approximately 0.25 Tm. Beam particle identification is performed using gas and aerogel threshold Cherenkov detectors. Identification of secondary particles is done by time-of-flight measurements in resistive plate chambers and by measuring the Cherenkov angle in an aerogel ring imaging detector based on the Belle-II design [16]. A lead calorimeter at the downstream end of the experiment enables the separation of electrons, muons, and hadrons. The total length of the spectrometer is approximately 2 m.

This paper presents the results of an EMPHATIC test-beam measurement made in January 2018 using only silicon strip detectors to record particle trajectories. No magnet and no detectors for secondary particle identification were used in the test-beam setup. The results include differential cross sections for p + C → X$^\pm$ at 20, 30, and 120 GeV/c, where X$^\pm$ is a single charged particle within 20 mrad, the acceptance of the tracking detectors used in this measurement. This enables the measurement of forward scattering (coherent elastic and quasielastic interactions). The event topology with a single forward charged particle includes coherent-elastic interactions, quasielastic interactions, and some production interactions. Coherent elastic interactions are defined as scattering off the whole nucleus. Both the incident particle and the target nucleus survive in this case. In quasielastic interactions, the target nucleus is fragmented while the incident hadron survives. Finally, production interactions are those in which at least one new meson is produced. Often, quasielastic and

production interactions are together categorized as inelastic interactions. We have also fit a simple model to our data to extract useful quantities such as total and elastic cross sections. Results are compared to both Monte Carlo predictions and existing measurements.

III. EXPERIMENTAL SETUP

The EMPHATIC test-beam measurements were done at the FTBF. The facility provides a primary 120 GeV/c proton beam from the main injector or a secondary beam with momentum above 2 GeV/c. The beam is delivered in 4 s spills every minute. The intensity is tunable from 1 to 100 kHz, and the typical beam spot area is 2 cm^2. The momentum resolution of the secondary beam ($\Delta p/p$) is approximately 2%. The FTBF provides a set of gas threshold Cherenkov detectors for secondary beam particle identification. Pion identification is possible above 5 GeV/c, while kaon identification is only possible above 18 GeV/c. The pressure in the first Cherenkov detector was tuned to detect positrons, muons, and pions in the secondary beam. The trigger includes signals from the first Cherenkov detector in the anti-coincidence with two scintillators to remove all particles except kaons and protons. The pressure in the second gas Cherenkov detector was tuned to detect kaons, which can be separated from the protons during data analysis.

The FTBF also provides a set of silicon strip detectors (SSDs) with an effective area of 3.8×3.8 cm^2 and a strip pitch of 60 μm. Each detector has two silicon strip planes for measuring two independent dimensions. Four detectors were placed upstream, and three were placed downstream from the target. In addition to silicon strip detectors, the FTBF provides a silicon pixel telescope consisting of eight

pixel planes located between four upstream SSDs and the target. Four of the planes have a sensitive area of 3.24×1.62 cm^2, and the other four have an area of 1.62×2.43 cm^2. Due to inefficiencies in the pixel data acquisition (DAQ) and the smaller effective area, data from the pixels are not used for this measurement. Instead, the pixel telescope is treated as a passive material in the beamline and the data are corrected for interactions in this material. The schematic overview of the setup with the defined coordinate system is shown in Fig. 1.

The target is made of Toyo Tanso IG-43 graphite, which is the target material of choice in the T2K beamline. The same graphite was used for NA61/SHINE measurements. The target thickness is 2 cm which is approximately 5% of the interaction length. The measured target density is 1.83 ± 0.04 g/cm^3.

IV. SIMULATION AND DATA ANALYSIS

The data collected with graphite and empty targets are summarized in Table I. The empty target data are used for silicon strip alignment and for estimating background interactions in data analysis. The alignment is done by selecting 10000 empty target events with a single hit per silicon strip plane. A simple line fit is used to fit a track in each event. The tracking plane positions and angles are determined by minimizing the sum of χ^2 values for all 10000 track fits. Any position misalignment is at submicron level and any angular misalignment is below 0.01 mrad.

After alignment, angular resolution is determined for each dataset by fitting tracks upstream and downstream of the target separately and calculating the angle between them in x-z and y-z planes. The angular distributions of the tracks are fit with Gaussian functions, and the fitted widths
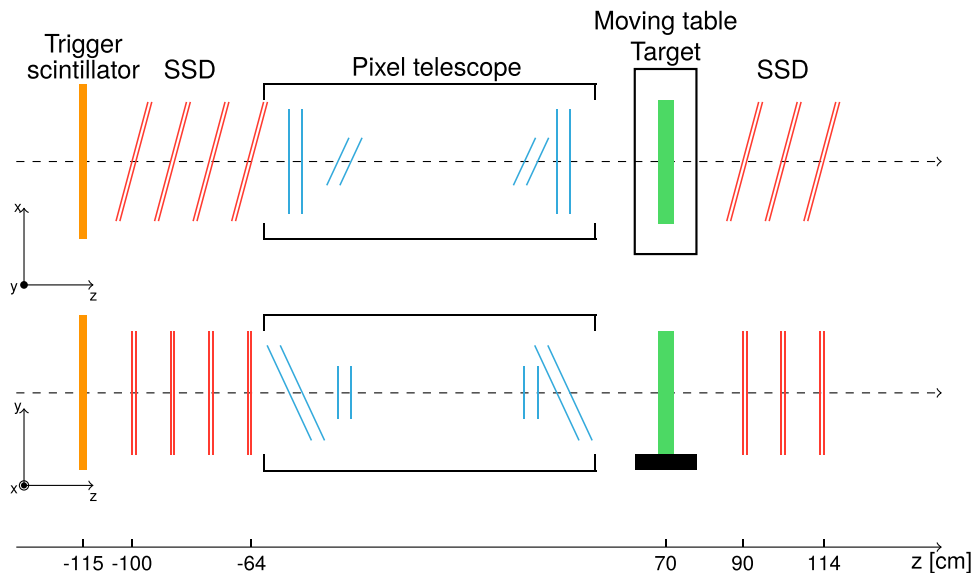

FIG. 1.   Schematic overview of the experimental setup: top view (top) and side view (bottom). The first trigger scintillator and gas Cherenkov detectors are located several meters upstream, and are not shown.

TABLE I.   Collected number of triggers.

p (GeV/c)	Target	Number of triggers (10^6)
20	Carbon	0.463
20	Empty	0.410
30	Carbon	1.031
30	Empty	0.197
120	Carbon	1.013
120	Empty	1.068

divided by $\sqrt{2}$ are taken as the effective angular resolution. The effective angular resolution includes the intrinsic angular resolution of the detector and the smearing effect caused by multiple scattering in the detector material. Multiple scattering decreases with momentum ($1/p$ dependence), and the effective resolution for 120 GeV/c data approaches the intrinsic angular resolution equal to 0.05 mrad (see Fig. 2). Additionally, we estimated x and y position resolutions at the interaction point. The interaction point (z_{int}) is defined as a z position where the distance between upstream and downstream tracks ($d = \sqrt{\Delta x^2 + \Delta y^2}$) is minimal. The position resolution is extracted by fitting Gaussians to Δx and Δy distributions at z_{int}. The values are 204, 145, and 66 μm for 20, 30, and 120 GeV/c graphite target data, respectively.

Silicon strip efficiencies are also calculated based on the empty target data. For a given silicon strip plane, events are selected by requiring a single cluster per plane in all other planes. A track is fitted for each event, extrapolated to the selected plane and checked if there is a cluster present within ±60 μm. The efficiencies are better than 99%. Both the angular resolution for different datasets and silicon plane mean efficiencies are presented in Fig. 2.

The positions and efficiencies of the silicon strip planes obtained from these studies, as well as beam-profile measurements from the data, are used as input parameters

in GEANT4-based Monte Carlo simulation [17]. Angular distributions from the data are used to validate the simulation. The simulation includes silicon strip and pixel planes, target, and trigger scintillators. In total, 10 million beam protons are simulated for each beam setting with FTFP_BERT and QGSP_BERT physics lists from GEANT4.10.05.p01. The simulation is used to estimate detector acceptance, reconstruction inefficiencies, and corresponding corrections are applied to data. Additionally, simulated events are used for some of the systematic studies described in Sec. VI.

The measurement of the forward differential cross section without final-state momentum measurement is based on the assumption that four-momentum transfer t is approximately equal to $t \approx -p_{\text{b}}^2 \theta^2$ for small t, where p_{b} is the incident beam momentum, and θ is the scattering angle. This approximation is valid for coherent elastic and quasielastic interactions. However, it cannot be used for inelastic scattering. The measurements presented here include proton-carbon differential cross sections for events with a single charged particle emitted from the target within ±20 mrad with respect to the beam particle. Such interactions also include inelastic scattering where, for example, a neutron and pion are emitted, but only the pion is detected. Therefore, the approximation for t does not hold for these events. It is possible to remove inelastic events by applying an undesirable model-dependent correction. Instead, we report $d\sigma/d(p_{\text{b}}^2 \theta^2)$:

$$\left(\frac{d\sigma}{d(p_{\text{b}}^2 \theta^2)}\right)_i = \frac{1}{N_{\text{pot}}} \frac{N_i}{nd \cdot \Delta(p_{\text{b}}^2 \theta^2)_i}, \quad (1)$$

where N_{pot} is the number of protons on target, N_i is the measured number of events with a single downstream track in a $p_{\text{b}}^2 \theta^2$ bin i corrected for detector efficiency and
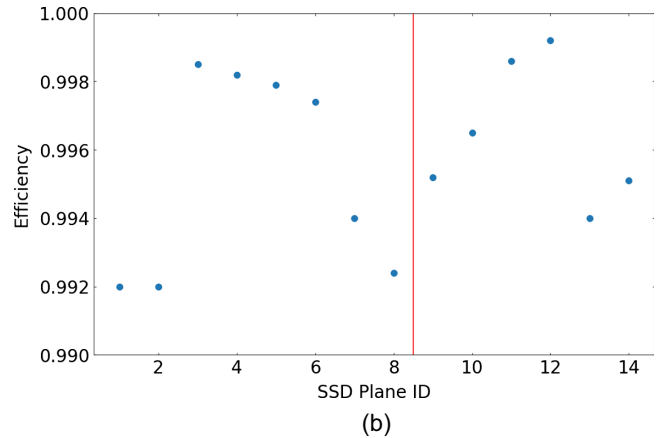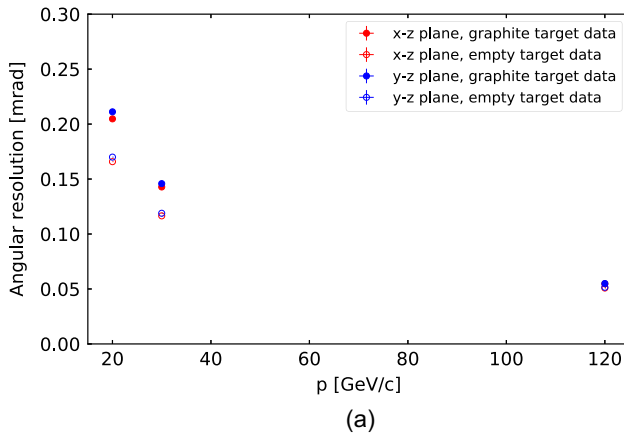

FIG. 2.   The effective angular resolution vs beam momentum (a) and mean silicon strip plane efficiencies (b). The angular resolution is shown for both, the empty and the carbon target data. Multiple scattering in the target makes the effective angular resolution in the carbon target data worse at low momentum. The vertical red line in the efficiency plot separates upstream and downstream planes. The planes are ordered starting from the most upstream plane (1) and ending with the most downstream plane (14).

acceptance, $nd = 0.000179$ mb^{-1} is the target number density multiplied by the target length and $\Delta(p_b^2 \theta^2)_i$ is ith bin width. A set of cuts is applied to the data to remove any background interactions.

A. Event selection

Event selection is divided into upstream and downstream track selection. The purpose of the former is to select a pure proton sample and to remove any interactions upstream from the target. The purpose of the latter is to select a pure sample of events with a single scattered charged particle downstream of the target.

Beam particle identification is done using gas Cherenkov detectors available. One detector used in anti-coincidence with the trigger scintillator is used to remove pions and electrons in the beam. The gas pressure in the second detector was set above the kaon threshold. Kaons and any electrons and pions remaining are removed by cutting out the signal in the recorded analog to digital converter (ADC) distribution, as shown in Fig. 3. Protons are part of the pedestal since they did not produce any Cherenkov light. The average number of photoelectrons detected from kaons passing through the detector is around 30. Nonproton contamination is estimated by fitting the kaon signal and integrating the signal function under the selected region of the pedestal (between dashed lines in Fig. 3). The signal function is a weighted sum of Gaussians with weights calculated according to the Poisson distribution. The contamination is less than 0.1%. The 120 GeV/c beam is a pure proton beam since it comes directly from the main injector, and Cherenkov detectors are not necessary in this case.

Additional cuts are applied to remove most of the interactions in the upstream silicon strips and the scintillator trigger. Only events with a single upstream track with a cluster in each plane and a sufficiently low χ^2 are selected. Additionally, events with tracks in the tails of the beam divergence distributions are removed since these are mostly coming from upstream interactions. After these selection
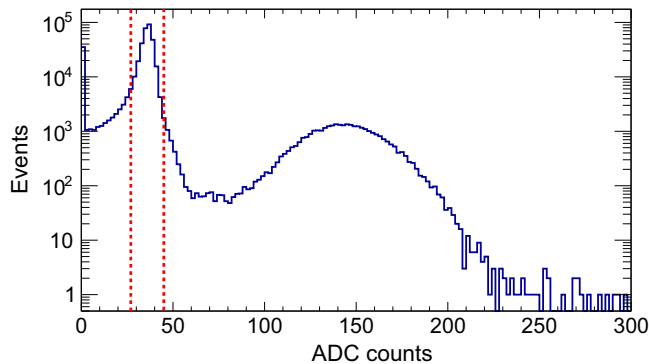
criteria are applied, the estimated number of upstream interactions remains below 0.1%. However, these do not include interactions in the silicon pixel layers that are between the upstream strip layers and the target. Finally, a cut is applied to the incoming beam particle so that scattered particles within ± 20 mrad always fall within the acceptance of the downstream silicon strip layers.

The downstream selection aims to identify forward-scattered beam protons and remove events with hard inelastic interactions in the pixel telescope, target, and downstream SSDs. Selected events have only one reconstructed track with a hit cluster in each downstream plane and the χ^2 value below 6 (see Fig. 4). An additional cut is applied to remove interactions in silicon pixel layers. The upstream and downstream tracks in an event are extrapolated toward the center of the target. A cut is applied on the x and y distances between the tracks. If an interaction happened somewhere outside of the target, the difference in x and y positions would be larger. The cut on the x and y distances is defined as

$$|x_{\text{up}} - x_{\text{down}}| > 3 \cdot \sigma_x + 3 \cdot \sigma_{\theta_x} \cdot |z_{\text{vert}} - z_{\text{targ}}| \quad (2a)$$

$$|y_{\text{up}} - y_{\text{down}}| > 3 \cdot \sigma_y + 3 \cdot \sigma_{\theta_y} \cdot |z_{\text{vert}} - z_{\text{targ}}|, \quad (2b)$$

where $\sigma_{x(y)}$ is a width of the $x(y)$ distance distribution and $\sigma_{\theta_{x(y)}}$ is a width of $\theta_{x(y)}$ distribution. A schematic of the x and y cuts is shown in Fig. 5.

To illustrate the effect of the x and y cuts, a reconstructed angle vs reconstructed vertex position distribution is shown in Fig. 6 before and after applying the cuts. Several peaks are
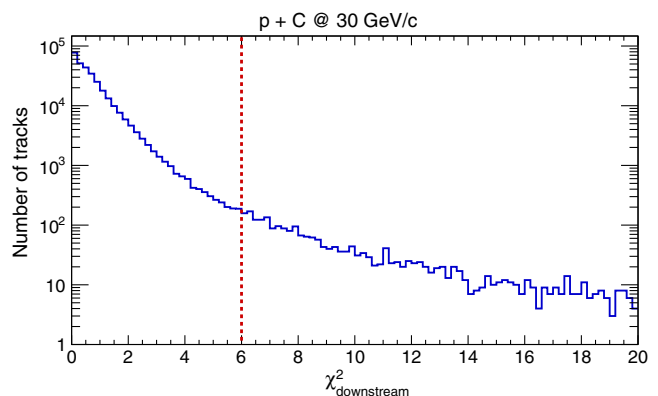

FIG. 4. The downstream χ^2 distribution for 30 GeV/c data. Values are obtained from fitting the straight line trajectories to the downstream silicon strip data. Events are discarded in analysis if $\chi^2 > 6$ which is denoted by a red line. According to Monte Carlo, a significant fraction of downstream tracks with $\chi^2 > 6$ underwent elastic scattering in downstream silicon strips. Noninteracting events in the χ^2 distribution tail underwent significant multiple scattering and are also in the tails of θ_x and θ_y angular distributions. Such events degrade both position and angular resolution and are removed.

FIG. 3. The ADC count distribution for the photomultiplier tube in the second gas Cherenkov detector for 30 GeV/c data. Selected events are located between dashed red lines.
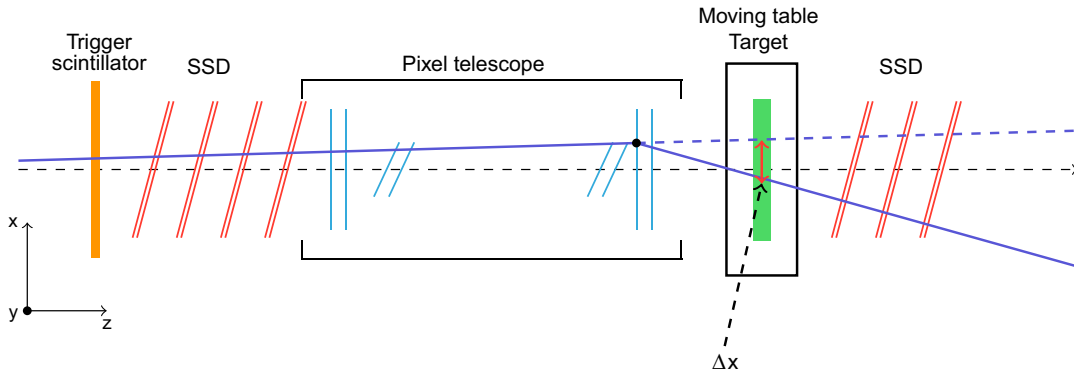
FIG. 5. A schematic of the x and y cut. If interaction happens in a pixel plane, x and y distances between upstream and downstream tracks at target z position will be significantly different than zero.

visible in the distribution. The first peak from the left corresponds to the last upstream silicon strip plane. The next four peaks correspond to the eight pixel planes (which are paired and separated by 5 cm). The most prominent peak corresponds to interactions in the target. The last peaks correspond to the first downstream silicon strip plane. After

x and y cuts are applied, inelastic interactions outside of the target are removed in both data and simulation.

The raw differential cross section needs to be corrected for various effects, such as SSD inefficiencies, reconstruction and selection inefficiencies, and interactions outside of the target. The efficiency corrections can be
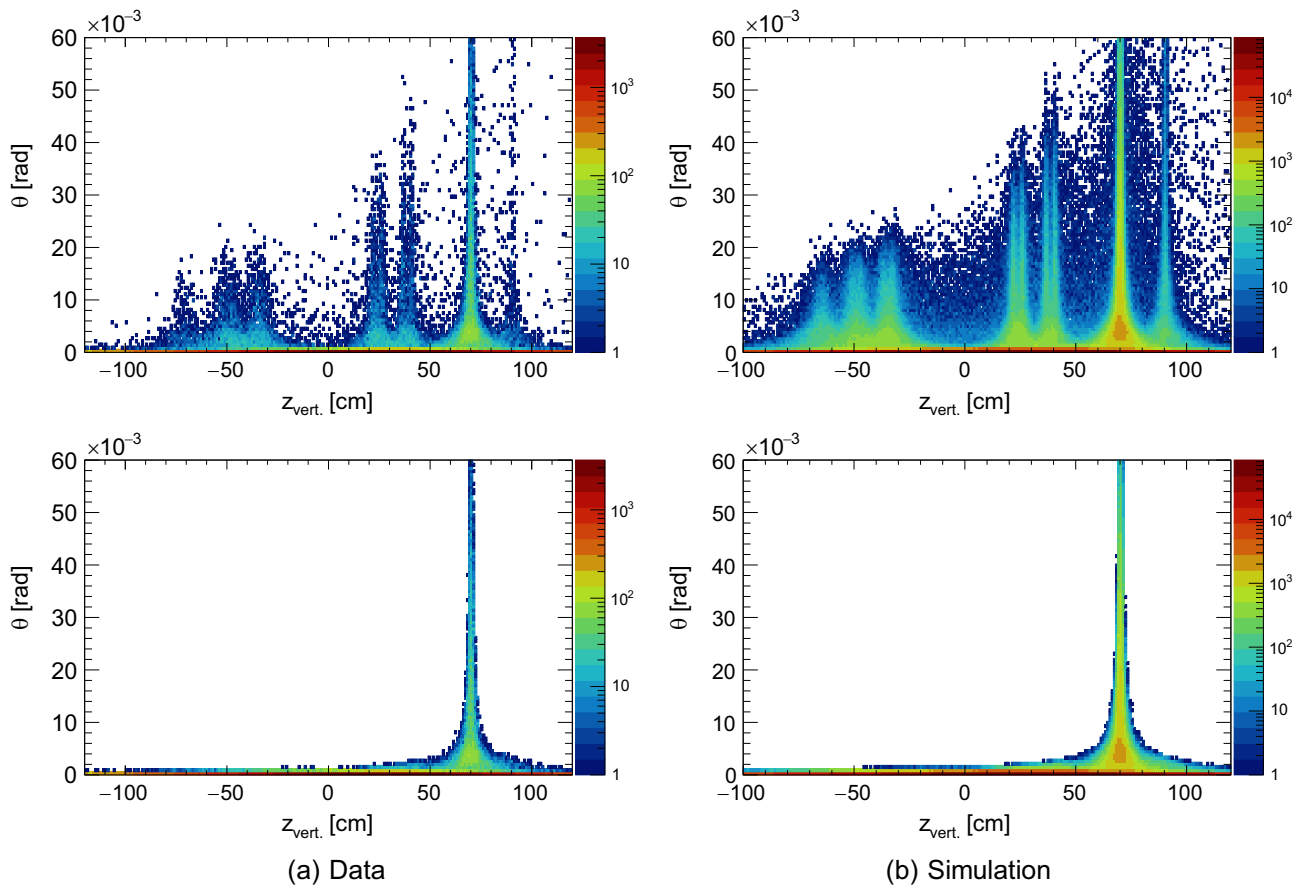

(a) Data

(b) Simulation

FIG. 6. Reconstructed angle vs reconstructed vertex z position for proton-carbon data (a) and FTFP_BERT G4.10.04.p2 Monte Carlo (b) at 30 GeV/c before (top) and after (bottom) x and y cuts. The first peak at $z = -70$ cm shows interactions in the last upstream silicon plane. The next four peaks are in fact four double peaks (clearly visible in simulation) and they show interactions in eight pixel planes. The large peak at $z = 70$ cm includes interactions in the target, and the last peak includes interactions in the first downstream silicon strip detector.
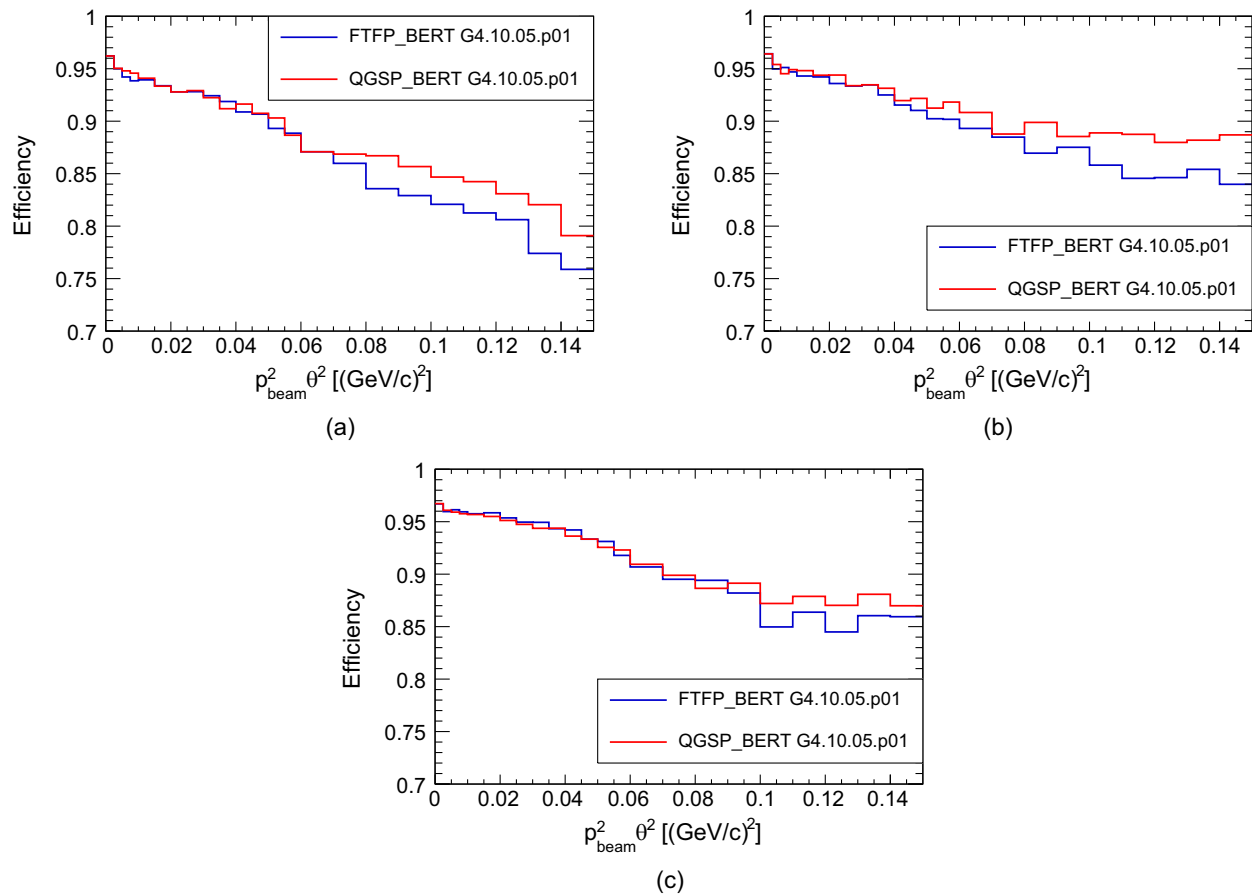
FIG. 7. Downstream selection efficiency for proton-carbon data at 20 GeV/c (a), 30 GeV/c (b), and 120 GeV/c (c) for FTFP_BERT and QGSP_BERT G4.10.05.p1 physics lists.

categorized as follows: corrections based on Monte Carlo simulation and corrections based on data.

B. Monte Carlo correction factors

The Monte Carlo correction factor includes silicon strip efficiency, reconstruction efficiency, and selection efficiency. However, it does not include smearing effects caused by detector resolution. The efficiency factor is defined as

$$\epsilon_i = \frac{N_{i,\text{sel,true}}}{N_{i,\text{true}}}, \qquad (3)$$

where i is the $p^2\theta^2$ bin number, $N_{i,\text{sel,true}}$ is the number of selected downstream tracks in the true bin i, and $N_{i,\text{true}}$ is the number of true tracks in the bin i before the selection. The efficiency is calculated only for beam particles hitting the target without any prior interaction. The correction factor is defined as an inverse efficiency. A GEANT4-based Monte Carlo simulation has been used to calculate these factors. The simulation includes the target, silicon strip detectors, silicon pixel detectors, and the trigger scintillator. Two physics lists are used to calculate the

correction factors: FTFP_BERT and QGSP_BERT from Geant4.10.05.p1. Monte Carlo efficiency is presented in Fig. 7. Differences in efficiency between datasets come from differences in the fraction of inelastic events. Selected events with a single forward low momentum charged proton or pion tend to have lower efficiency. The probability of scattering in downstream tracking layers and multiple scattering increases for low momentum particles. Therefore the χ^2 of these tracks tends to be higher on average, resulting in lower efficiency.

C. Data correction factors

Pixel interactions removed by Δx and Δy cuts are elastic interactions with higher four-momentum transfer and inelastic interactions. In the case of inelastic pixel interactions, particles reaching the target will have a significantly changed momentum and might not be protons. On the other hand, elastic interactions keep the original particle intact with a slight change in momentum. Still, the measured $p^2\theta^2$ will be significantly affected even though most of these particles do not interact with the carbon target. The downstream selection removes these events from measured $p^2\theta^2$ distribution, but the normalization (the

total number of protons on target) also needs to be adjusted. A normalization correction is subtracted from the number of incoming beam particles. The correction is estimated from the empty target data to avoid any bias from including interactions in the target:

$$N_{\text{POT,cor}} = N_{\text{tout,rem}} \cdot C \cdot \frac{N_{\text{tin,POT}}}{N_{\text{tout,POT}}}, \qquad (4)$$

where $N_{\text{tout,rem}}$ is the number of removed pixel interactions in the empty target data, C is the purity correction based on simulation, and $\frac{N_{\text{tin,POT}}}{N_{\text{tout,POT}}}$ is the ratio of number of selected events after upstream selection in the carbon target and empty target data. The purity correction is a ratio of the true removed pixel interactions and the total number of removed events. The normalization correction is 2.0%, 2.3%, and 3.0% for 20, 30, 120 GeV/c data respectively.

V. SYSTEMATIC UNCERTAINTIES

Several systematic uncertainties are considered in the analysis: beam purity, the number of interactions in upstream detectors (beam loss), target density and thickness uncertainties, and efficiency variations. As previously mentioned, kaon contamination in the proton beam after gas Cherenkov cut is estimated to be negligible. Beam loss is caused by interactions in the pixel telescope, as explained in the previous section. Since the beam loss is between 2% and 3% and the purity correction is around 95%, any systematic uncertainty is going to be small. The beam loss systematic contribution includes the statistical uncertainty from the empty target data and purity variation estimated by using FTFP_BERT and QGSP_BERT physics lists. Values are below 1% for all three datasets. A normalization uncertainty from the measured target density and thickness is estimated to be 2%, and it is the dominant contribution at low $p^2\theta^2$.

The efficiency uncertainty includes contributions from Monte Carlo (MC) statistics, SSD plane efficiencies, differences in χ^2 distributions between data and MC, differences in angular resolution, and model differences. Silicon efficiencies in the simulation are reduced in all planes by their uncertainties, and the efficiency is reevaluated. The difference between the nominal and reevaluated efficiency is taken as a systematic uncertainty.

A similar approach is used for the variation of cut parameters. The χ^2 distribution from the data has a longer tail compared to the distribution from the simulation. This is caused by a small number of track clusters with multiple active strips in data. These clusters are created by delta (knock-on) electrons. Delta electrons induce signals in the neighboring strips and create a systematic shift in the measured position of the original particle. Reconstructed tracks with such clusters will have increased χ^2 value. The χ^2 value used in the MC cut is

adjusted so that the fraction of removed events is the same as the one in the data. The efficiency is reevaluated after using the new cut, and the difference is taken as a systematic uncertainty.

Similarly, the angular resolution in Monte Carlo simulation can be from 3% to 7% different from the data, depending on the dataset. Angular resolution parameters in Δx and Δy cuts are varied within $\pm 7\%$, and the difference is taken as a systematic uncertainty.

Finally, the differences in efficiency estimated with FTFP_BERT and QGSP_BERT are used as a systematic uncertainty. These differences are caused by the variation in the number of events with a single low momentum pion in the forward direction. Low momentum pions (< 5 GeV/c) have lower selection efficiency compared to elastically scattered beam particles. Effective angular resolution for these pions is worse due to an increase in multiple scattering. Therefore, these pions will be over-represented in the tail of the angular distribution, or they will have increased χ^2 values. The difference between models is largest for higher $p^2\theta^2$ values because of the higher fraction of low momentum pions.

Two codominant contributions to the efficiency uncertainty are coming from SSD efficiency variations and angular resolution differences and are between 1% and 2%. The total efficiency uncertainty is between 2% and 3%, and it is the dominant systematic uncertainty contribution at higher $p^2\theta^2$.

VI. DIFFERENTIAL CROSS-SECTION RESULTS

Differential cross-section results are presented in Fig. 8. Comparisons with FTFP_BERT and QGSP_BERT physics lists are also included. Both physics lists give similar predictions with significant differences compared to the data. The prediction is typically lower (up to 40%) compared to the data. In older versions of GEANT4 (v4.9.06), the proton-nucleus cross section is extracted from the chiral invariant phase space (CHIPS) dataset. However, in more recent versions, this dataset has been replaced with the Barashenkov-Glauber-Gribov dataset. We have also included comparisons with the modified FTFP_BERT (G4.10.05) physics list that includes CHIPS cross sections. Since this change only affects the total cross section, the predictions that use the CHIPS dataset differ only in the elastic region and show slightly better agreement with the data. Total, statistical, and systematic uncertainties for 30 GeV/c data are also presented in Fig. 9 as an example, while all results are summarized in tables available in [18].

A. Model fits

To compare our results with previous data, it is necessary to extract total, coherent-elastic and inelastic cross sections. Typically, the total cross section can be extracted via a transmission measurement in which the number of
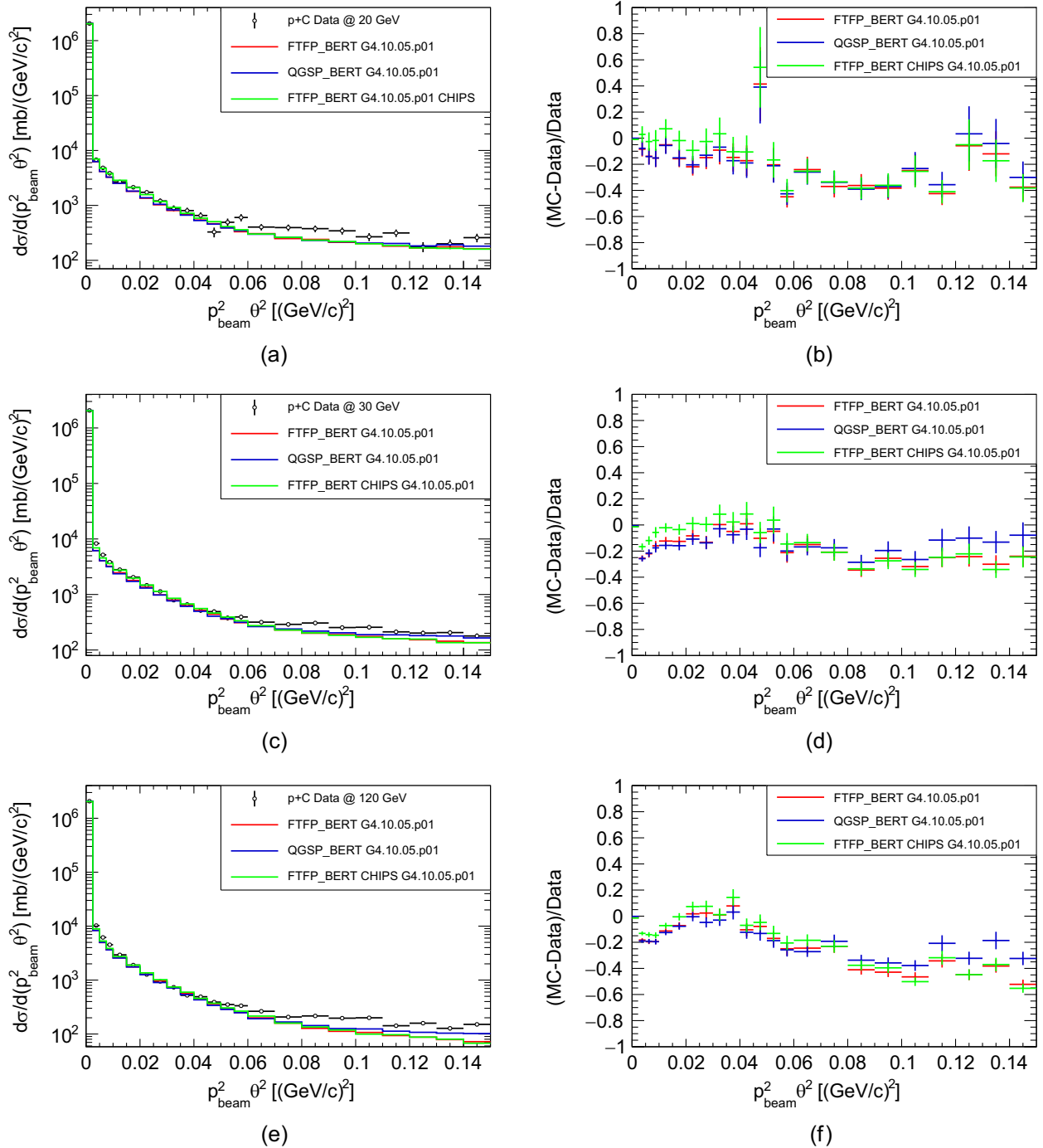
FIG. 8. The p + C differential cross section at 20 GeV/c (a), 30 GeV/c (c), and 120 GeV/c (e), and their corresponding comparisons to the FTFP_BERT and QGSP_BERT models from GEANT 4.10.05.p01 (b), (d), and (f).

surviving beam particles is related to the total cross section:

$$N_S = N_0 e^{-nd\sigma_{\text{tot}}}, \qquad (5)$$

where N_S is the number of surviving beam particles, N_0 is the initial number of beam particles, nd is the target number density multiplied by the target thickness, and σ_{tot} is the total cross section. An alternative approach is to measure

the differential cross section and use the optical theorem to extract the total cross section. The optical theorem states that the total cross section is proportional to the imaginary part of the scattering amplitude at $t = 0$ GeV^2. An advantage of EMPHATIC is the ability to perform a combined measurement using both techniques since all interacting and noninteracting events have been recorded.
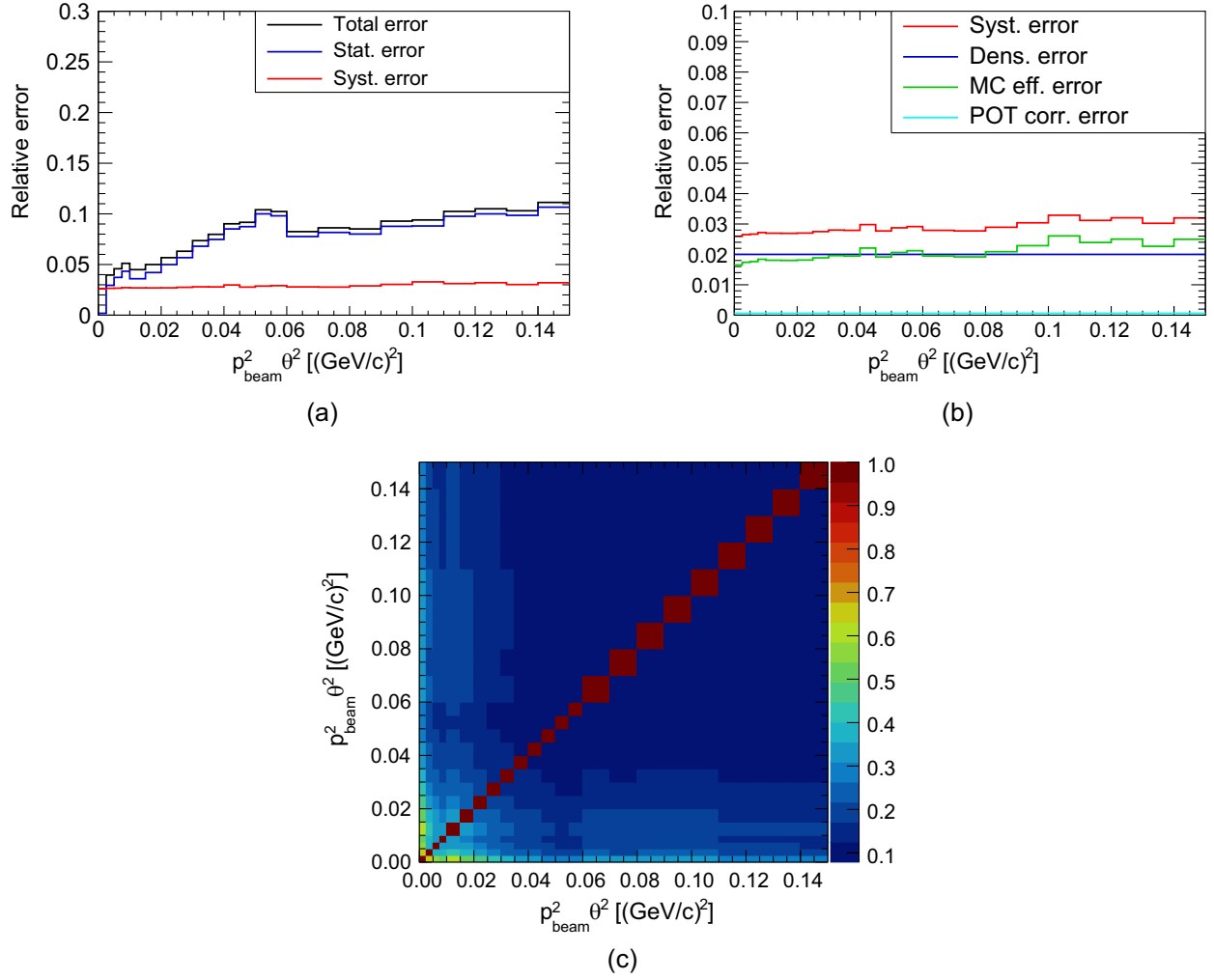
(a)

(b)

(c)

FIG. 9.   The total, statistical and systematic uncertainty for p + C differential cross section at 30 GeV/c (a) and different contributions to the systematic uncertainty (b), and correlation matrix (c).

Coherent elastic and quasielastic proton-carbon interactions are governed by nonperturbative QCD, and there are no simple QCD predictions for our measurements. However, we have fitted a simple phenomenological model to the data to extract the desired parameters. Similar models have been used in many older measurements, such as [19] and more recently in proton-proton interactions in the ATLAS experiment [20,21]. The full model used in the fit is

$$M(p^2\theta^2; A, B, B_{pN}, B_I, \sigma_{\text{tot}}, \sigma_{\text{tot},pN}, C, \Lambda) = \frac{1}{16\pi}\left(\frac{\sigma_{\text{tot}}}{\hbar c}\right)^2 (1 + \rho^2) e^{-Bp^2\theta^2} \tag{6a}$$

$$+ \frac{1}{16\pi}\mathcal{H}(p^2\theta^2 - \Lambda)\left(\frac{8\pi\alpha Z_1 Z_2 \hbar c}{p^2\theta^2}\right)^2 e^{-Bp^2\theta^2} \tag{6b}$$

$$- 2\frac{1}{16\pi}\mathcal{H}(p^2\theta^2 - \Lambda)(\rho\cos\Delta\Phi + \sin\Delta\Phi)\frac{\sigma_{\text{tot}}}{\hbar c}\frac{8\pi\alpha Z_1 Z_2 \hbar c}{p^2\theta^2} e^{-Bp^2\theta^2} \tag{6c}$$

$$+ N(A) \cdot \frac{1}{16\pi}\left(\frac{\sigma_{\text{tot},pN}}{\hbar c}\right)^2 e^{-B_{pN}p^2\theta^2} \tag{6d}$$

$$+ \frac{1}{16\pi}\left(\frac{C}{\hbar c}\right)^2 e^{-B_I p^2\theta^2} \tag{6e}$$

$$+ \mathcal{H}(10^{-4}[\text{GeV}^2] - p^2\theta^2)\frac{1}{nd \times 10^{-4}[\text{GeV}^2]} e^{-(\sigma_{\text{tot}} + \sigma_{C-el} + \sigma_C)\cdot n\cdot d}. \tag{6f}$$
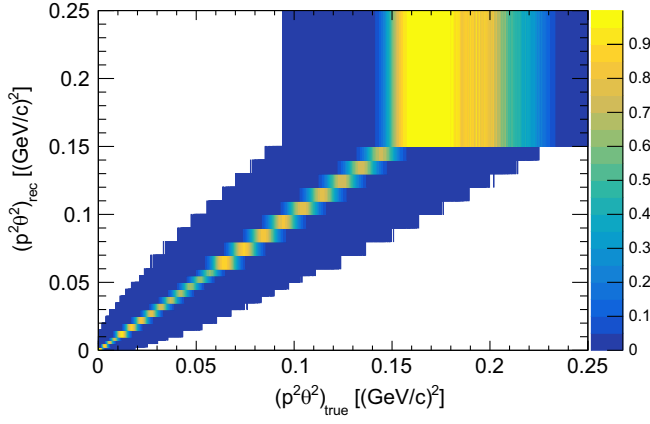
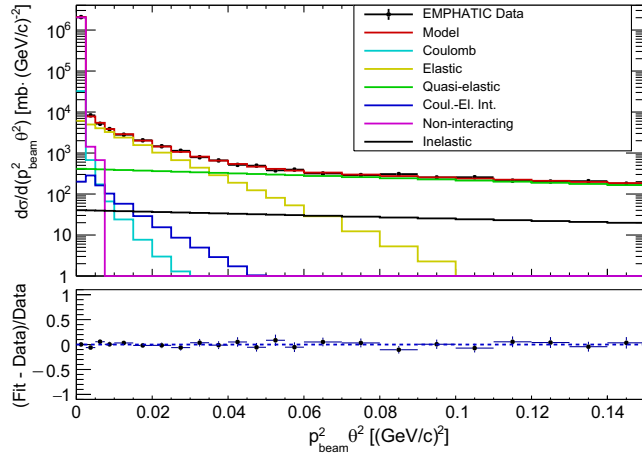FIG. 10.   The migration matrices for 30 GeV/c data.

FIG. 11.   The model fit for 30 GeV/c data.

The model assumes that the nucleon distribution inside the carbon nucleus follows the normal distribution and the coherent-elastic differential cross section [Eq. (6a)] is an exponential function of the four-momentum transfer ($t \approx p^2\theta^2$). The normalization is determined by the optical theorem and relates to the total cross section σ_{tot}, while the exponential parameter B is proportional to the sum of squares of proton and nuclear radii. Often, it is assumed that the coherent nuclear amplitude is purely imaginary. However, this is not well measured, and we assume a small

real amplitude as well. The ratio of the real to the imaginary part of the amplitude is denoted as ρ.

The Coulomb differential cross section [Eq. (6b)] is a simple Rutherford formula with the exponential form factor. It is assumed that the carbon nuclear charge density follows the nucleon distribution. This assumption follows from work by Kopeliovich and Tarasov [22]. The Coulomb scattering is divergent at $t = 0$ GeV^2, and we include a cutoff parameter Λ to remove the divergence.

Possible interference between coherent-elastic and Coulomb scattering is included in the third line of Eq. (6). Interference is zero if the nuclear amplitude is purely imaginary. However, we have already assumed that this is not the case. In addition, the nuclear amplitude gains a modifying phase $\Delta\Phi$ due to the presence of the Coulomb field.

Quasielastic interactions are defined as elastic interactions on a single nucleon. Therefore, the quasielastic differential cross section [Eq. (6d)] will have the same t dependence as the coherent-elastic differential cross section, but only with different parameters. The effective number of nucleons visible to a beam proton is denoted as $N(A)$.

Inelastic contamination [Eq. (6e)] in our measurements is mostly coming from events with a single forward charged particle (mostly pions). We assume that such background mostly comes from Δ resonance production. Moreover, the GEANT4 simulation suggests that the background is almost flat in $p^2\theta^2$ or has an exponential shape with a small slope. Therefore, we assume the same functional dependence as coherent-elastic and quasielastic differential cross sections, only with different parameters.

Finally, noninteracting contributions [Eq. (6f)] are calculated using Eq. (5). Instead of using only the total nuclear proton-carbon cross section, we have also integrated Eqs. (6b) and (6c) to obtain the total effective cross section. The number of surviving particles is normalized to obtain the same dimension as the differential cross section. The Heaviside step function ensures that surviving beam particles are only placed in the first true $p^2\theta^2$ bin (0–10^{-4} GeV^2).

The full model is first smeared to account for bin migration. Migration matrices are generated from empty target data and the GEANT4 simulation of the multiple scattering in the target (see Fig. 10). The χ^2 is minimized by

TABLE II.   Best fit parameter values and their uncertainties.

p (GeV/c)	Parameter	B [(GeV)$^{-2}$]	B_{pN} [(GeV)$^{-2}$]	B_I [(GeV)$^{-2}$]	σ_{tot} (mb)	$N(A) \cdot \sigma_{\text{tot},pN}$ (mb)	C (mb)	ρ	Λ [(GeV)$^{-2}$]
20	Value	80.9	7.1	5.0	344.3	201.8	19.0	-0.13	2.0×10^{-5}
	Statistical error	7.1	3.7	2.7	12.3	25.2	40.0	Fixed	Fixed
30	Value	85.1	6.5	4.9	362.8	182.7	10.1	-0.13	2.0×10^{-5}
	Statistical error	4.1	1.3	2.7	8.2	27.1	47.7	Fixed	Fixed
120	Value	79.3	5.8	5.0	335.9	143.2	23.8	-0.13	2.0×10^{-5}
	Statistical error	2.9	1.2	4.7	6.7	20.5	30.9	Fixed	Fixed

TABLE III.   Extracted cross sections and elastic slopes.

p (GeV/c)	Parameter	B [(GeV)$^{-2}$]	σ_{tot} (mb)	σ_{el} (mb)	σ_{inel} (mb)
20	Value	80.9	344.3	74.7	269.3
	Statistical error	7.1	12.3	8.4	14.9
	Systematic error (low)	-1.6	-10.0	-2.86	-7.1
	Systematic error (high)	$+2.5$	$+11.7$	$+3.0$	$+10.2$
30	Value	85.1	362.8	79.1	283.8
	Statistical error	4.1	8.2	5.2	9.7
	Systematic error (low)	-1.5	-10.0	-3.0	-7.0
	Systematic error (high)	$+3.1$	$+12.2$	$+2.8$	$+9.6$
120	Value	79.3	335.9	72.7	263.3
	Statistical error	2.9	6.7	3.9	7.8
	Systematic error (low)	-3.9	-15.6	-3.2	-9.3
	Systematic error (high)	$+2.4$	$+9.1$	$+2.0$	$+7.0$

varying the model parameters. The relative phase $\Delta\Phi$ is not an independent parameter, and it is taken from the calculation by Kopeliovich and Tarasov [22]. The ρ parameter is set to be a constant with a value of -0.13, taken from [23]. Since $N(A)$ and $\sigma_{\text{tot},pN}$ appear only as a product, they are merged into a single parameter. An example of the fit for 30 GeV/c data is presented in

Fig. 11. Since the inelastic background has the same functional $p^2\theta^2$ dependence as the quasielastic differential cross section and they are similar in size, the corresponding fit parameters have large uncertainties. Therefore, we are not confident in reporting these values as meaningful physical results. Best fit values for all parameters are summarized in Table II.
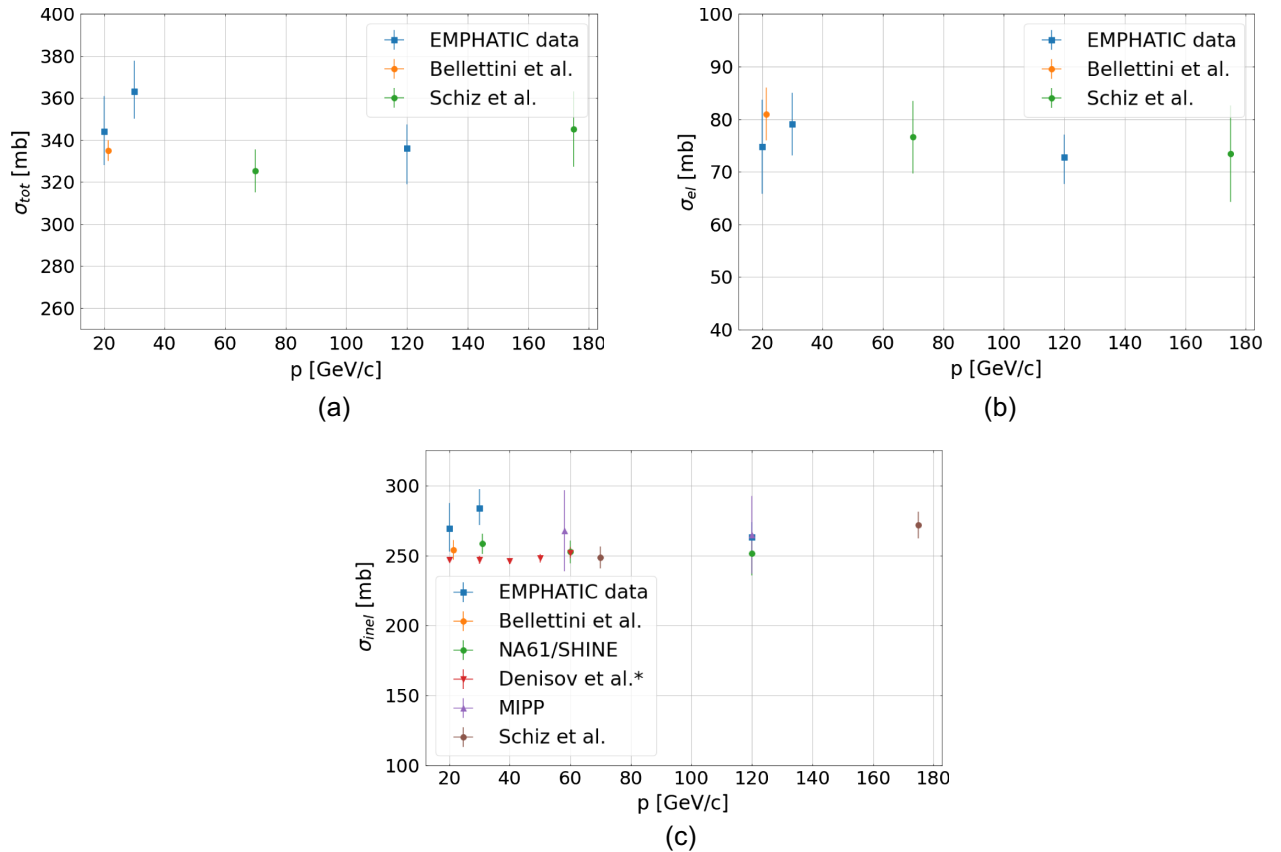

FIG. 12.   Comparisons of the total (a), elastic (b), and inelastic cross section (c) obtained from the fits with older data. The total cross section is compared to the data from Bellettini *et al.* [19]. The elastic cross section is compared to values obtained from Bellettini *et al.* [19] and Schiz *et al.* [26]. The inelastic cross section is compared to the results from Bellettini *et al.* [19], NA61/SHINE collaboration [4,6], Denisov *et al.* [27], and MIPP collaboration [28].

However, we present measurements of the elastic slope B, the total cross section σ_{tot}, the total coherent elastic cross section σ_{el}, and the total inelastic cross section σ_{inel}. The total coherent elastic cross section σ_{el} is calculated by integrating Eq. (6a). Additionally, the total inelastic cross section is estimated as $\sigma_{\text{tot}} - \sigma_{el}$. To estimate systematic uncertainties, fits are repeated in different configurations. The ρ parameter is varied between -0.20 and -0.05, according to [23]. The migration matrix is recalculated by using the Highland approximation [24,25] of the multiple scattering in the target:

$$\theta_0 = \frac{13.6 \text{ MeV}}{\beta c p} z \sqrt{\frac{x}{X_0}} \left[1 + 0.038 \log\left(\frac{x}{X_0}\right) \right]. \quad (7)$$

The initial value of the Λ parameter is varied within its uncertainty and fixed during the fit. The value of Λ is 2×10^{-5} GeV^2 for all datasets. The values of the extracted cross sections, elastic slopes B, and their uncertainties for different datasets are summarized in Table III.

A comparison of the cross-section results with the older measurements is presented in Fig. 12. The statistical and systematic uncertainties of the extracted cross sections are similar in size. The main reason for the large systematic uncertainty comes from the variation of the ρ parameter. Unfortunately, our current data and methods do not allow us to extract the ρ parameter with any precision due to the large migration between the first four upstream bins. To improve this in the future, we will reduce the migration effect by reducing the material budget. Additionally, removing inelastic backgrounds by using a momentum measurement will allow us to measure the quasielastic cross section.

VII. SUMMARY AND FUTURE MEASUREMENTS

We have measured the forward differential cross section in proton-carbon interaction at 20, 30, and 120 GeV/c as a function of $p^2\theta^2$ with a simple setup consisting of silicon strip detectors. These results feature a novel technique that uses both transmission measurement and the optical theorem to extract the cross section. Future EMPHATIC runs will use a permanent magnet for momentum measurements, allowing us to remove the inelastic background currently included in the results. Additionally, we will remove the primary source of dead material (pixel planes) and thus reduce both efficiency and normalization systematic uncertainties. Finally, a high DAQ rate of 30 kHz will allow us to record many different datasets and create a cross-section table for the crucial interactions contributing to the neutrino flux in various experiments.

[1] K. Abe *et al.* (Hyper-Kamokande Proto-Collaboration), arXiv:1805.04163.

[2] B. Abi *et al.*, J. Intrum. **15**, T08008 (2020).

[3] K. Abe *et al.* (T2K Collaboration), Phys. Rev. D **87**, 012001 (2013); **87**, 019902(A) (2013).

[4] N. Abgrall *et al.* (NA61/SHINE Collaboration), Eur. Phys. J. C **76**, 84 (2016).

[5] N. Abgrall *et al.* (NA61/SHINE Collaboration), Eur. Phys. J. C **76**, 617 (2016).

[6] A. Aduszkiewicz *et al.* (NA61/SHINE Collaboration), Phys. Rev. D **100**, 112001 (2019).

[7] N. Abgrall *et al.* (NA61/SHINE Collaboration), Eur. Phys. J. C **79**, 100 (2019).

[8] M. Apollonio *et al.* (HARP Collaboration), Nucl. Phys. **A821**, 118 (2009).

[9] M. Apollonio *et al.* (HARP Collaboration), Phys. Rev. C **80**, 035208 (2009).

[10] J. M. Paley *et al.* (MIPP Collaboration), Phys. Rev. D **90**, 032001 (2014).

[11] A. V. Lebedev, Ratio of pion kaon production in proton carbon interactions, Ph.D. thesis, Harvard University, 2007.

[12] S. M. Seun, Measurement of $\pi - K$ ratios from the NuMI target, Ph.D. thesis, Harvard University, 2007.

[13] B. Abi *et al.*, Eur. Phys. J. C **80**, 978 (2020).

[14] G. D. Barr, T. K. Gaisser, S. Robbins, and T. Stanev, Phys. Rev. D **74**, 094009 (2006).

[15] T. Akaishi *et al.* (EMPHATIC Collaboration), arXiv:1912.08841.

[16] L. Burmistrov *et al.*, Nucl. Instrum. Methods Phys. Res., Sect. A **958**, 162232 (2020).

[17] S. Agostinelli *et al.*, Nucl. Instrum. Methods Phys. Res., Sect. A **506**, 250 (2003).

[18] M. Pavin *et al.* (EMPHATIC Collaboration), arXiv:2106.15723.

[19] G. Bellettini, G. Cocconi, A. Diddens, E. Lillethun, G. Matthiae, J. Scanlon, and A. Wetherell, Nucl. Phys. **79**, 609 (1966).

[20] L. Adamczyk (ATLAS Collaboration), Proc. Sci. DIS2015 (**2015**) 061.

[21] M. Aaboud *et al.* (ATLAS Collaboration), Phys. Lett. B **761**, 158 (2016).

[22] B. Kopeliovich and A. Tarasov, Phys. Lett. B **497**, 44 (2001).

[23] B. Kopeliovich and T. Trueman, Phys. Rev. D **64**, 034004 (2001).

[24] V. L. Highland, Nucl. Instrum. Methods **129**, 497 (1975).

[25] G. R. Lynch and O. I. Dahl, Nucl. Instrum. Methods Phys. Res., Sect. B **58**, 6 (1991).

[26] A. M. Schiz, Hadron-nucleus scattering at 70-GeV/c, 125-GeV/c and 175-GeV/c and a high statistics study of hadron-proton elastic scattering at 200-GeV/c, Ph.D. thesis, Yale Universtiy, 1979.

[27] S. P. Denisov, S. V. Donskov, Yu. P. Gorin, R. N. Krasnokutsky, A. I. Petrukhin, Yu. D. Prokoshkin, and D. A. Stoyanova, Nucl. Phys. **B61**, 62 (1973).

[28] S. Mahajan and R. Raja (MIPP Collaboration), in Meeting of the APS Division of Particles and Fields (2013), arXiv:1311.2258.